

PAPER

Multiple triple-point fermions in Heusler compounds

To cite this article: Ranjan Kumar Barik *et al* 2018 *J. Phys.: Condens. Matter* **30** 375702

View the [article online](#) for updates and enhancements.

Related content

- [Topological semimetals predicted from first-principles calculations](#)
Hongming Weng, Xi Dai and Zhong Fang
- [Molybdenum Carbide: A Stable Topological Semimetal with Line Nodes and Triply Degenerate Points](#)
Jian-Peng Sun, Dong Zhang and Kai Chang
- [Electronic properties of topological insulator candidate CaAgAs](#)
Jayita Nayak, Nitesh Kumar, Shu-Chun Wu *et al.*



IOP | ebooks™

Bringing you innovative digital publishing with leading voices to create your essential collection of books in STEM research.

Start exploring the collection - download the first chapter of every title for free.

Multiple triple-point fermions in Heusler compounds

Ranjan Kumar Barik¹, Ravindra Shinde¹ and Abhishek K Singh¹

Materials Research Center, Indian Institute of Science, Bangalore 560012, India

E-mail: abhishek@iisc.ac.in

Received 24 March 2018, revised 6 July 2018

Accepted for publication 8 August 2018


Published 22 August 2018



Abstract

Using the density functional theoretical calculations, we report a new set of topological semimetals X_2YZ ($X = \{\text{Cu, Rh, Pd, Ag, Au, Hg}\}$, $Y = \{\text{Li, Na, Sc, Zn, Y, Zr, Hf, La, Pr, Pm, Sm, Tb, Dy, Ho, Tm}\}$ and $Z = \{\text{Mg, Al, Zn, Ga, Y, Ag, Cd, In, Sn, Ta, Sm}\}$), which show the existence of multiple topological triple point fermions along four independent \tilde{C}_3 axes. These fermionic quasiparticles have no analogues elementary particle in the standard model. The angle-resolved photoemission spectroscopy is simulated to obtain the exotic topological surface states and the characteristic Fermi arcs. The inclusion of spin-orbit coupling splits the triple-point to two Dirac points. The triple-point fermions are exhibited on the easily cleavable (1 1 1) surface and are well separated from the surface $\bar{\Gamma}$ point, allowing them to be resolved in the surface spectroscopic techniques. This intermediate linearly dispersive degeneracy between Weyl and Dirac points may offer prospective candidates for quantum transport applications.

Keywords: topological materials, triple point fermion, semimetals

 Supplementary material for this article is available [online](#)

(Some figures may appear in colour only in the online journal)

Quantum topological materials have been at the forefront of the intense research in condensed matter physics and materials science in recent years, as they exhibit fundamentally new physical phenomena with potential applications for novel devices [1–6]. The topological insulator, for instance, was the first three-dimensional (3D) topological material to be predicted and discovered [2, 7–10]. This was subsequently followed by the experimental observations of Weyl semimetals (WSMs) [3, 5, 11–16]. The recent research in nontrivial topological materials has been focused on the gapless materials, because of linear band crossings and the existence of exotic fermions as quasiparticles.

The topological semimetals (TSMs) are classified based on dimensionality and degeneracy of band crossings. A nodal point (zero-dimensional crossing) with two- and four-fold band degeneracy characterizes the Weyl and Dirac semimetals (DSMs), [17–19] respectively, while a nodal line (one-dimensional crossing) gives the corresponding nodal-line

semimetals [20, 21]. The band crossing points of WSMs, known as Weyl nodes, have definite integer chirality, and they always appear in pairs. The WSMs also exhibit peculiar surface states, known as Fermi arcs, which connects a pair of surface-projected Weyl nodes with opposite chirality. DSMs with four-fold band degeneracy can be thought of as a special case of WSM with merged Weyl nodes with zero effective chirality. Nodal-line semimetals are considered as a precursor for other topological phases: they can evolve into Weyl points, convert into Dirac points, or become a topological insulator by the introduction of the spin-orbit coupling (SOC) or mass term [22].

More recently, the classification mentioned above of fermions has been expanded to accommodate the triply-degenerate nodal points. This three-fold degeneracy gives rise to what is known as triple-point (TP) fermions [23–32] and has been confirmed experimentally [29]. These peculiar TP fermions do not have analog in the standard model of the high energy physics, so the existing topological invariants will not be applicable in contrast to the Dirac and Weyl nodes [29].

¹ Equal contribution.

Thus, these materials are expected to show new topological phenomena, transport behaviors, and spectroscopic responses, not present in DSMs and WSMs.

The TP fermions having novel band crossings have triggered the search of quantum topological materials, mainly because of exotic topological properties. Many candidate materials in different space groups have been predicted to show this feature [29], specifically with the crystal structures having three-fold rotational symmetry. In this paper, we predict a set of Heusler topological materials X_2YZ with characteristic TP fermions, which are present even in the absence of SOC. With the inclusion of collinear spin SOC, the TP splits into two separate Dirac points. The two distinct observed TPs shift anti-parallel with the change in the row of constituent atoms offering tunability. The electronic structure and topological properties of a representative Ag_2TmMg material are described in detail here; the corresponding properties of rest of the materials are given in the supporting information (stacks.iop.org/JPhysCM/30/375702/mmedia).

1. Methodology

The calculations were performed using the first-principles density functional theory (DFT) [33] as implemented in the Vienna *ab initio* simulation package (VASP) [34, 35]. Projector augmented wave (PAW) [36, 37] potentials were used to represent the ion–electron interactions. The electronic exchange and correlation were approximated by the generalized gradient approximation (GGA) using Perdew–Burke–Ernzerhof (PBE) type of functionals [38]. The wave functions were expanded in a plane wave basis with an energy cut-off of 400 eV and a Γ -centered $12 \times 12 \times 12$ Monkhorst–Pack [39] \mathbf{k} -grid Brillouin zone sampling. The calculations were done both with and without spin–orbit coupling. The Bloch spectral functions (see equation (1)) and the Fermi surfaces of the slab (constructed by stacking a number of principal layers) were calculated based on the iterative Green’s function method [40] by obtaining the tight-binding Hamiltonian (see equation (2)) from the maximally localized Wannier functions [41], as implemented in the WannierTools package [42].

$$A(\mathbf{k}_{\parallel}, \omega) = -\frac{1}{\pi} \lim_{\eta \rightarrow 0^+} \text{ImTr} G_s(\mathbf{k}_{\parallel}, \omega + i\eta) \quad (1)$$

where, the slabs’s Green’s function is given by $G_s(\mathbf{k}_{\parallel}, \omega + i\eta) \simeq (\omega - \varepsilon_n^s)^{-1}$. The tight-binding Hamiltonian for the slab is represented by [42],

$$H_{mn}^{\text{slab}}(\mathbf{k}_{\parallel}) = \begin{pmatrix} H_{mn,11}(\mathbf{k}_{\parallel}) & H_{mn,12}(\mathbf{k}_{\parallel}) & \cdots & H_{mn,1n_s}(\mathbf{k}_{\parallel}) \\ H_{mn,21}(\mathbf{k}_{\parallel}) & H_{mn,22}(\mathbf{k}_{\parallel}) & \cdots & H_{mn,2n_s}(\mathbf{k}_{\parallel}) \\ \vdots & \vdots & \ddots & \vdots \\ H_{mn,n_s,1}(\mathbf{k}_{\parallel}) & H_{mn,n_s,2}(\mathbf{k}_{\parallel}) & \cdots & H_{mn,n_s,n_s}(\mathbf{k}_{\parallel}) \end{pmatrix} \quad (2)$$

where, m or n denotes the atom-orbital index, \mathbf{k}_{\parallel} denotes the 2D-slab momentum, and n_s denotes the number of principle layers in the slab [42]. The individual elements of the Hamiltonian are given by simple intra and interlayer tight-binding terms:

$$H_{mn,ij}(\mathbf{k}_{\parallel}) = \sum_{\mathbf{R}=\mathbf{R}_1, \mathbf{R}_2, (i-j)\mathbf{R}_3} e^{i\mathbf{k}_{\parallel} \cdot \mathbf{R}} H_{mn}(\mathbf{R}).$$

The WannierTools code employed here to obtain the tight-binding model requires orthogonal basis functions to construct the Hamiltonian. These orthogonal basis functions are taken from maximally localized Wannier functions (constructed from Bloch states by wannierization). Similar to any other Kohn–Sham Hamiltonian, this Hamiltonian will also lack screening and would affect the interlayer coupling in the slab.

2. Results and discussion

2.1. Crystal and electronic structure

Ag_2TmMg belongs to the face-centered cubic centrosymmetric crystal structure (figure 1(a) with $Fm\bar{3}m$ (No. 225) space group. Ag atoms occupy $8c$ ($3/4, 3/4, 3/4$) and $8c$ ($1/4, 1/4, 1/4$) Wyckoff positions, whereas, Mg and Tm atoms occupy $4b$ ($1/2, 1/2, 1/2$) and $4a$ ($0, 0, 0$) Wyckoff positions, respectively. The optimized lattice constant of this non-magnetic Heusler compound is 4.91 Å, with a -0.31 eV/atom formation energy. The dynamical stability of the structure was verified by computing the phonon dispersion (see supporting information). Figure 1(b) shows the bulk Brillouin zone and its projection on to the equivalent (111) surface. This crystal structure has three-fold rotational symmetry (\tilde{C}_3) along the [111] direction, and there are four such equivalent directions. The structure also has a mirror symmetry plane (\tilde{M}_x). Due to the \tilde{C}_3 rotation, the \tilde{M}_x plane is repeated twice. If ψ_1 , ψ_2 and ψ_3 are the eigenvectors of the \tilde{C}_3 operator, only ψ_3 follows eigenvalue equation of \tilde{M}_x operator. Hence, \tilde{C}_3 and \tilde{M}_x do not commute, implying that the two-fold band degeneracy can only be obtained if the eigenvalues for both ψ_1 and ψ_2 are the same. A triply-degenerate node occurs, when a singly-degenerate band ψ_3 and doubly-degenerate bands (ψ_1 and ψ_2) cross each other. The phonon dispersion (see figure 1(c)) also shows a peculiar crossing which is linearly dispersive as well as triply-degenerate. This indicates an occurrence of bosonic Weyl quasiparticles.

The band structure of Ag_2TmMg along high-symmetry lines in the absence of SOC is shown in figure 2(a). In the neighborhood of Fermi level, along the Γ – X direction, a non-degenerate band touches a doubly degenerate band at around -0.2 eV. The Γ point itself hosts a triply degenerate point at -0.05 eV as seen in the K – Γ – L segment of the band structure. When projected onto the (111) surface, the TP observed at the Γ point merges with the [111] axes, hence cannot be resolved experimentally. However, the other TPs, which are well separated from the Γ point, can be observed on this easily cleavable (111) plane. This separation of TPs from the Γ point implies the observation of stronger Fermi arcs, leading to the easy detection in the angle-resolved photoemission spectroscopic (ARPES) experiments. Owing to mirror symmetry plane \tilde{M}_x , three-fold rotational symmetry (\tilde{C}_3) and the combination of time-reversal (\tilde{T}) and inversion symmetry (\tilde{I}), the TPs observed are replicated six-times in the

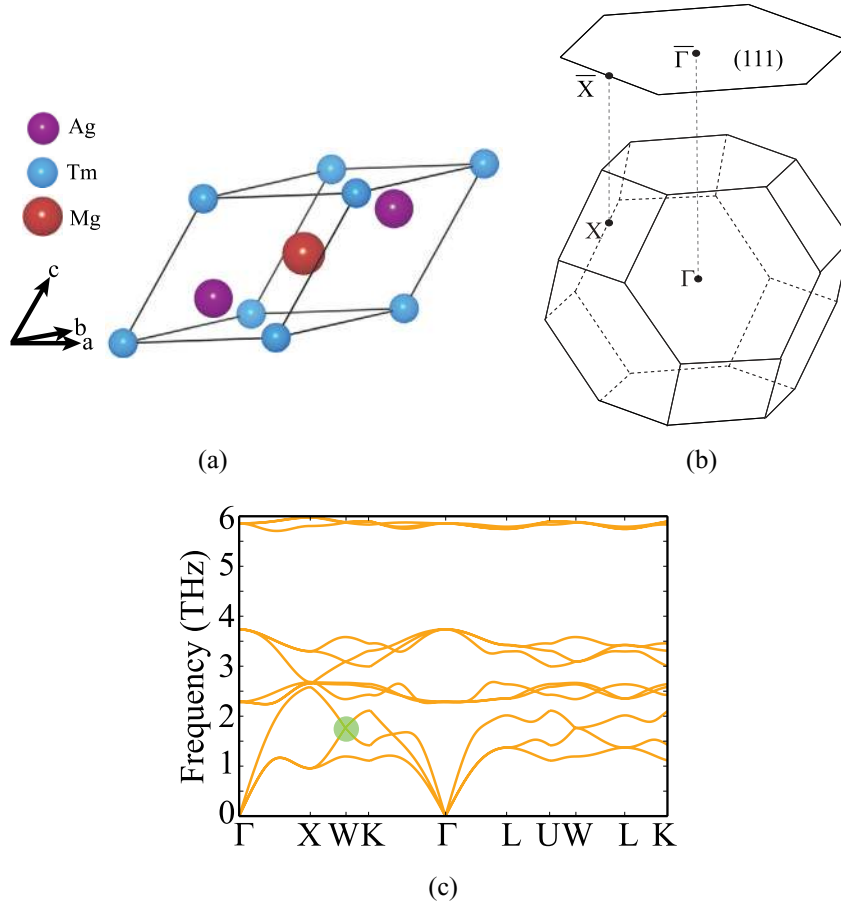


Figure 1. (a) The crystal structure of Ag_2TmMg compound with space group $Fm\bar{3}m$ (No. 225). (b) The corresponding 3D Brillouin zone along with its high-symmetry k-points and its projection onto the equivalent (1 1 1) surface. (c) The phonon dispersion.

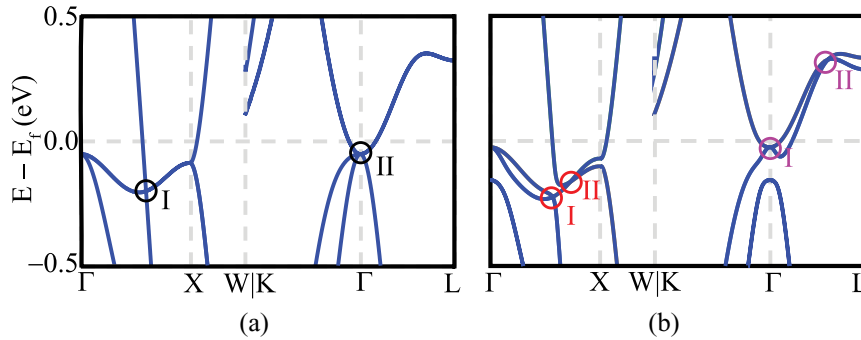


Figure 2. (a) The band structure of Ag_2TmMg without SOC showing the encircled triple points and (b) band structure with SOC. The triple points split in to two Dirac points with the inclusion of SOC.

Brillouin zone, making a hexagonal pattern. With the inclusion of SOC, these TPs split into two Dirac point of type-I and type-II along Γ -X as well as along Γ -L direction, as shown in the figure 2(b), implying that TPs in this class of materials are observed only in the absence of SOC.

In the case of Ag_2TmMg , the lighter element Mg was replaced with the same group elements and its effect was observed on the position of the two distinct TPs. Figure 3(a) shows the change in the location of TPs in the Brillouin zone for the different compounds. The TP1 (observed along the Γ -X segment) moves down with increasing row number of constituent elements, while TP2 moves upward. However, the variation is prominent

in the binding energy of TP1 as compared to that of TP2. This is surprising because the majority of the orbital contribution to the TPs comes from Ag and Tm only. In the case of Ag_2InX ($X = \text{Pr, Sm, Tb, Dy}$ and Lu) (see figure 3(b)), the binding energies of TP1 increases gradually with increase in atomic number of lanthanide elements, while the binding energy of TP2 remains at the Fermi level. Therefore, effectively, we can tune the position of TPs in the appropriately alloyed compound. Table 1 of supporting information shows the binding energies of TPs for each of the material studied. A wide variation is seen in the values of binding energies providing an avenue of composition-controlled tunable TPs.

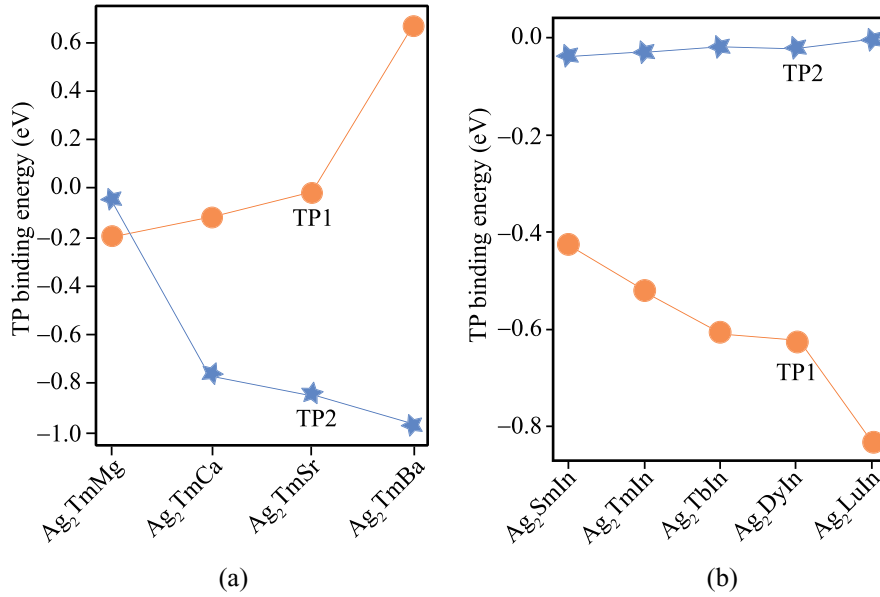


Figure 3. The variations of binding energies of TPs with the selected compounds in (a) Ag₂TmX alkaline earth family and, (b) Ag₂XIn lanthanide family. The variations of binding energies of TPs with the selected compounds.

2.2. Bloch spectral function and Fermi arcs

The surface-projected density of states (or Bloch spectral function) is calculated by iterative Green's function method, by obtaining the tight-binding Hamiltonian from the maximally localized Wannier functions. This function simulates the experimental angle-resolved photoemission spectroscopy, giving valuable information about the surface states and nodal points. In figure 4(a), bright yellow lines indicate the contribution from the surface states, and the TP is seen at the -0.2 eV and the two-thirds of momenta along Γ - X direction. These states are seen to merge on the linearly dispersing bands and crossing the TP. The corresponding surface-projected density of states in the neighbourhood of $\bar{\Gamma}$ in the \bar{K} - $\bar{\Gamma}$ - \bar{L} direction is as shown in figure 4(c). Slightly below the Fermi level, a TP is observed due to touching of non-linearly dispersing bands. This TP, however, cannot be resolved in surface measurements because of its location at the Γ point.

A three-fold rotational symmetry (\tilde{C}_3) along (111) direction is a crucial requirement for the existence of TPs. Since there are four such equivalent (111) directions, the TPs will appear in four pairs in the Brillouin zone. The SOC splits these TPs into two Dirac points of type-I and type-II along Γ - X as well as along Γ - L direction. The Dirac points, which are far away from Γ point (see figures 5(a), (b) and (d)) will form a hexagonal ring kind of Fermi surface by repeating each Dirac point six times in the whole Brillouin-zone due to \tilde{C}_3 and inversion symmetry, whereas the Dirac point appearing at Γ point (see figure 5(c)) forms a Fermi surface in a circular ring shape.

The TPs can also be characterized by the Fermi arcs on the surface Bloch spectrum. Since there are four equivalent (111) directions, the Γ point projection coincides with one of the TPs on the (111) surface. Hence, three other TPs and their time-reversal counterparts will be seen in an hexagonal pattern on the (111) surface (see figure 4(b)). The Fermi arcs

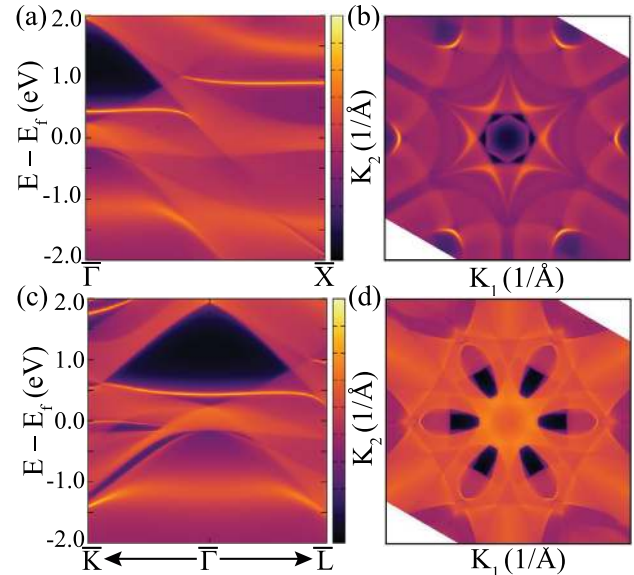


Figure 4. (a) The (111) Bloch spectral function depicting the surface states of Ag₂TmMg along the Γ - X segment. The dark yellow lines denote the surface contribution. (b) Fermi surface calculated with the chemical potential of -0.2 eV. (c) The (111) Bloch spectral function depicting the surface states of Ag₂TmMg near the Γ point. The dark yellow lines denote the surface contribution. (d) Fermi surface calculated with the chemical potential of -0.05 eV.

emanating from a given TP connect to the neighboring TPs forming a flower-like hexagonal Fermi surface. Again, this pattern is due to the three-fold rotational symmetry and time-reversal symmetry along the diagonal of the primitive unit cell. The Fermi surface corresponding to the $\bar{\Gamma}$ in the \bar{K} - $\bar{\Gamma}$ - \bar{L} segment (see figure 4(d)) shows a bright spot at the center connected by the arcs and the nearby six TPs at the vertices of the hexagon.

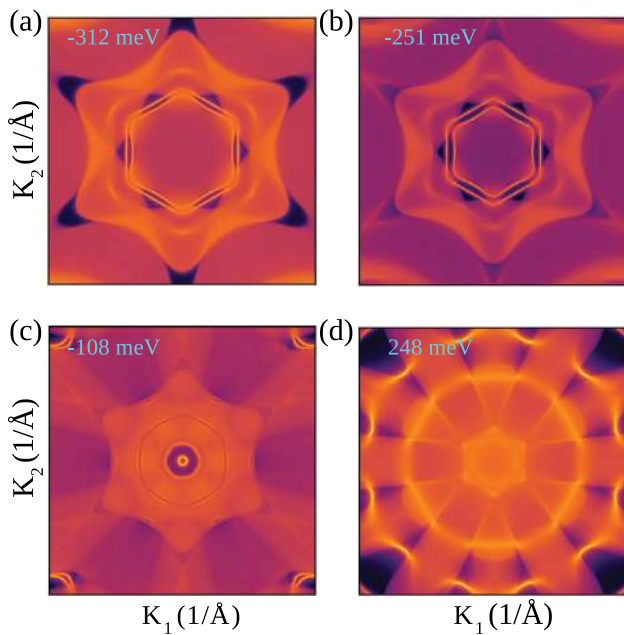


Figure 5. Fermi surface of Dirac points at various chemical potentials (a) and (b) along Γ -X direction (c) at Γ and (d) along Γ -L.

3. Conclusion

In conclusion, we have theoretically predicted several new materials hosting peculiar triple-point fermions as quasiparticles. Also, they show signature hexagonal Fermi arcs connecting the vertices to the center and the nearest vertex. This set of materials and the slab were particularly chosen to maximize the number of TPs and easy experimental preparation. Since all the six TPs are well separated from each other and are away from the Brillouin zone center, it offers easy detection using surface sensitive spectroscopic methods. The two distinct TPs observed shift anti-parallel with the change in the row of the constituent lighter atom, whereas the binding energy of one of the TPs observed in the lanthanide series remains almost zero throughout. This study can guide the experimental observation of triple-point fermions, based on the location of Fermi arcs. An appropriate alloying offers a possibility of tuning the position of the TPs. Additionally, not only electronic bands show triply-degenerate crossings, but also the phonon bands exhibit this characteristic behaviour. The TP fermions cannot be characterized by the conventional topological invariants, elucidating the complexity of this new class of topological materials. The observation of triply-degenerate nodal points and the Fermi arcs presented in this study help in the characterization of these exotic new class of topological materials.

Acknowledgments

The authors thank Dr Swaminathan Venkataraman for valuable discussions. RS acknowledges Science and Engineering Research Board, DST, India for a fellowship (PDF/2015/000466). This work is partly supported by the US.

Army Contract FA5209-16-P-0090. We also acknowledge Materials Research Center and Supercomputer Education and Research Center, Indian Institute of Science for providing computational facilities.

Supporting information

The list of materials, along with their phonon dispersion, band structures (with and without SOC) and the binding energies of TPFs are given in the supporting information.

ORCID iDs

Ranjan Kumar Barik <https://orcid.org/0000-0002-0639-4130>
Ravindra Shinde <https://orcid.org/0000-0001-5182-1480>
Abhishek K Singh <https://orcid.org/0000-0002-7631-6744>

References

- [1] Bernevig B A, Hughes T L and Zhang S C 2006 *Science* **314** 1757–61
- [2] Moore J E 2010 *Nature* **464** 194–8
- [3] Wan X, Turner A M, Vishwanath A and Savrasov S Y 2011 *Phys. Rev. B* **83** 205101
- [4] Yang K Y, Lu Y M and Ran Y 2011 *Phys. Rev. B* **84** 075129
- [5] Xu G, Weng H, Wang Z, Dai X and Fang Z 2011 *Phys. Rev. Lett.* **107** 186806
- [6] Ojanen T 2013 *Phys. Rev. B* **87** 245112
- [7] Hasan M Z and Kane C L 2010 *Rev. Mod. Phys.* **82** 3045–67
- [8] Qi X L and Zhang S C 2011 *Rev. Mod. Phys.* **83** 1057–110
- [9] Fu L, Kane C L and Mele E J 2007 *Phys. Rev. Lett.* **98** 106803
- [10] Hsieh D *et al* 2009 *Science* **323** 919–22
- [11] Burkov A A and Balents L 2011 *Phys. Rev. Lett.* **107** 127205
- [12] Singh B, Sharma A, Lin H, Hasan M Z, Prasad R and Bansil A 2012 *Phys. Rev. B* **86** 115208
- [13] Weng H, Fang C, Fang Z, Bernevig A B and Dai X 2015 *Phys. Rev. X* **5** 011029
- [14] Xu S Y *et al* 2015 *Science* **349** 613–7
- [15] Xu S Y *et al* 2015 *Science* **347** 294–8
- [16] Huang S M *et al* 2015 *Nat. Commun.* **6** 7373
- [17] Young S M, Zaheer S, Teo J C Y, Kane C L, Mele E J and Rappe A M 2012 *Phys. Rev. Lett.* **108** 140405
- [18] Wang Z, Sun Y, Chen X Q, Franchini C, Xu G, Weng H, Dai X and Fang Z 2012 *Phys. Rev. B* **85** 195320
- [19] Wang Z, Weng H, Wu Q, Dai X and Fang Z 2013 *Phys. Rev. B* **88** 125427
- [20] Kim Y, Wieder B J, Kane C L and Rappe A M 2015 *Phys. Rev. Lett.* **115** 036806
- [21] Yu R, Weng H, Fang Z, Dai X and Hu X 2015 *Phys. Rev. Lett.* **115** 036807
- [22] Yu R, Fang Z, Dai X and Weng H 2017 *Frontiers Phys.* **12** 127202
- [23] Wieder B J, Kim Y, Rappe A M and Kane C L 2016 *Phys. Rev. Lett.* **116** 186402
- [24] Bradlyn B, Cano J, Wang Z, Vergniory M G, Felser C, Cava R J and Bernevig B A 2016 *Science* **353** 6299
- [25] Winkler G W, Wu Q S, Troyer M, Krogstrup P and Soluyanov A A 2016 *Phys. Rev. Lett.* **117** 076403
- [26] Weng H, Fang C, Fang Z and Dai X 2016 *Phys. Rev. B* **93** 241202
- [27] Zhu Z, Winkler G W, Wu S Q, Li J and Soluyanov A A 2016 *Phys. Rev. X* **6** 031003

- [28] Weng H, Fang C, Fang Z and Dai X 2016 *Phys. Rev. B* **94** 165201
- [29] Chang G et al 2017 *Sci. Rep.* **7** 1688
- [30] Zhang T T, Yu Z M, Guo W, Shi D, Zhang G and Yao Y 2017 *J. Phys. Chem. Lett.* **8** 5792–7
- [31] Xia Y and Li G 2017 *Phys. Rev. B* **96** 241204
- [32] Yang H, Yu J, Parkin S S P, Felser C, Liu C X and Yan B 2017 *Phys. Rev. Lett.* **119** 136401
- [33] Kohn W and Sham L J 1965 *Phys. Rev.* **140** A1133
- [34] Kresse G and Furthmüller J 1996 *Comput. Mater. Sci.* **6** 15–50
- [35] Kresse G and Furthmüller J 1996 *Phys. Rev. B* **54** 11169–86
- [36] Blöchl P E 1994 *Phys. Rev. B* **50** 17953–79
- [37] Kresse G and Joubert D 1999 *Phys. Rev. B* **59** 1758–75
- [38] Perdew J P, Burke K and Ernzerhof M 1996 *Phys. Rev. Lett.* **77** 3865–8
- [39] Monkhorst H J and Pack J D 1976 *Phys. Rev. B* **13** 5188–92
- [40] Sancho M P L, Sancho J M L, Sancho J M L and Rubio J 1985 *J. Phys. F* **15** 851–8
- [41] Mostofi A A, Yates J R, Pizzi G, Lee Y S, Souza I, Vanderbilt D and Marzari N 2014 *Comput. Phys. Commun.* **185** 2309–10
- [42] Wu Q, Zhang S, Song H F, Troyer M and Soluyanov A A 2018 *Comput. Phys. Commun.* **224** 405–16